ELSEVIER

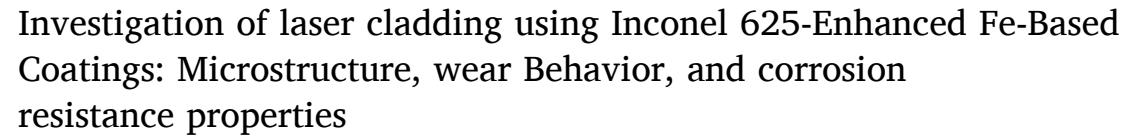
Contents lists available at ScienceDirect

Applied Surface Science

journal homepage: www.elsevier.com/locate/apsusc



Full Length Article





Yiqi Wang, Tianbiao Yu, Jiayu Sun, Yingying Zhang, Zhengyu Sun, Chong Yu, Jiahui Yin

School of Mechanical Engineering and Automation, Northeastern University, Shenyang, China

ARTICLE INFO

Keywords: Laser cladding Fe-Inconel 625 composite coatings Ductile iron Corrosion resistance Wear behavior

ABSTRACT

To improve the surface quality, corrosion resistance, and wear resistance of ductile iron (DI), laser cladding technology was utilized to deposit Fe-based alloy with varying amounts of Inconel 625 (0 wt% 15 wt% and 30 wt%) onto DI substrates. This study aimed to achieve an optimal balance between cost-efficiency and performance. The coatings were fabricated using a six-pass, three-layer laser cladding process and systematically evaluated through electrochemical corrosion tests, hardness measurements, and wear resistance assessments. Advanced microstructural analyses, including elemental distribution and phase characterization, were performed employing optical microscopy (OM), X-ray diffraction (XRD), scanning electron microscopy (SEM), and energy dispersive spectroscopy (EDS). Results revealed that adding an appropriate amount of Inconel 625 effectively eliminated interfacial whitening. The Fe-based coating with 30%wt Inconel 625 exhibited superior corrosion resistance and a hardness of 304 HV, approximately 1.7 times higher than that of the substrate. Furthermore, the wear mechanism transitioned from abrasive wear to adhesive wear with the incorporation of Inconel 625. This study provides a scientific foundation for optimizing the surface quality of Fe-Inconel625 coatings via laser cladding, highlighting promising advancements in material properties for corrosion and wear resistant applications.

1. Introduction

Ductile iron (DI) is widely regarded as a critical structural material in various engineering disciplines, owing to its high strength, excellent formability, and cost effectiveness[1,2]. Nevertheless, its limited corrosion resistance in moist environments significantly reduces its service life and restricts potential applications[3–5]. Since corrosion affects the material's surface, applying protective coatings to DI surfaces presents a practical solution to mitigate this issue.

The corrosion and wear characteristics of high-performance materials are crucial for their durability and long-term sustainability. In efforts to enhance these properties, researchers have extensively explored surface modification techniques for DI. Among these, laser cladding has emerged as a highly promising technology, owing to its efficiency, flexibility, and the creation of a narrow heat-affected zone, which facilitates strong metallurgical bonding while minimizing substrate dilution [6–8]. As advancements in oceanic exploration expanded the demand for corrosion-resistant materials, the development of Fe-based coatings tailored for harsh marine environments has become imperative. Recent studies have provided valuable insights into improving the corrosion resistance of Fe-based coatings. For example, Luo et al. [9]

investigated FeAl laser cladding coatings with varying chromium content and demonstrated that chromium additions significantly enhance corrosion resistance through solid solution hardening and grain refinement. Similarly, Gao et al. [10] examined the impact of varying Fe levels in laser-cladded Ni60 coatings, revealing that corrosion resistance initially decreased but subsequently improved with increased Fe content, suggesting a cost-effective approach to enhance the performance of these coatings in abrasive conditions.

The varied composition of cladding materials and substrates introduces complexities into the laser cladding process for cast iron. In this process, the morphology and size of the graphite, along with the types of compounds produced, significantly influence the resultant material properties [11]. Several studies have investigated the application of laser cladding to repair DI components and enhance surface performance. For instance, Li et al. [12] utilized Ni-Cu alloy powders for surface remanufacturing of DI, revealing that the shape and size of graphite, as well as the nature of the compounds formed, substantially affect the resulting material properties. Chen et al. [13] analyzed the corrosion behavior of DI in NaCl solution and demonstrated that chloride ions (Cl-) accelerate longitudinal corrosion, ultimately resulting in perforation failure. Additionally, Weng et al. [14] explored the impact of

varying laser power levels on crack susceptibility in Fe-based coatings for DI substrates. Poloczek et al. [15] enhances Inconel625-based composite coatings with TiC particles to increase hardness. Poloczek et al. [16] further pointed out that the incorporation of TiC was found to form a composite microstructure with Ti, Nb, Mo and C-rich particles precipitating during crystallization. Yan et al. [17] fabricated Fe-based composite layers reinforced with TiC and Cr, demonstrating that the complete dissolution of graphite nodules facilitated the formation of fine primary and compound dendrites, which enhancing wear resistance. Similarly, the corrosion resistance of Ni-resist DI can be improved through laser surface alloying (LSA), which extended the solubility of alloying elements, produced finer dendrites, and eliminated spheroidal graphite [18].

The corrosion resistance and mechanical properties of Fe-Inconel 625 laser-cladded coatings in NaCl environments has not been thoroughly examined. This study aims to address this gap by investigating the wear and corrosion resistance of Fe-based coatings through laser cladding on DI substrates with the addition of Inconel 625.

2. Materials and methods

2.1. Material and method

The material used in this study comprised an Fe-based alloy powder (Fe105) and a Ni-based alloy powder (Inconel 625), both with a purity exceeding 99.5 % and a particle size range of 100–270 $\mu m.$ To ensure a homogeneous mixture, these powders were subjected to ball milling for 2 h at 200 rpm, maintaining a ball-to-powder weight ratio of 10:1. Prior to the laser cladding experiments, the powders were dried in a vacuum oven at 120 $^{\circ} C$ for 2 h to eliminate moisture and enhance flowability. The substrate employed was ductile cast iron QT 500, measuring 100 mm \times 100 mm \times 10 mm.

The chemical compositions of the substrate and powders are presented in Table 1-3. The corresponding content and particle morphologies of the samples are presented in Fig. 1, Fig. 2 and Table 4, respectively. The powders' particle sizes were within the operational limits of the powder feeder, ensuring stable flow and minimizing deposition defects. The experimental setup comprised a coaxial laser direct energy deposition (LDED) system [19], as illustrated in Fig. 2. The continuous wave (CW) fiber laser source operated at a maximum power of 500 W and a wavelength of 1020 nm, with a Gaussian beam focused at a 55 mm focal length. The cladding head was positioned 15 mm from the laser focus, where the laser beam achieves a diameter of 1.0 mm. A three-layer, six-pass coating strategy with laser power at 405 W, scanning speed at 3 mm/s, powder feeding rate at 0.8 r/min, overlapping ratio at 50 % and Z-axis lifting amount at 388 μm was adopted for all experiments. Prior to coating deposition, the precursors were dried at 100 °C for 2 h to eliminate residual moisture. Additionally, substrate preparation included abrasion with SiC grit sandpapers(400#-1500#), polishing with diamond paste, subsequently cleaning with alcohol to remove contaminants.

2.2. Characterization

Following the laser cladding process, specimens were sectioned using a wire-cutting technique to produce samples measuring 15 mm \times 5 mm \times 10 mm for microstructural analysis and high-temperature corrosion testing. Standard metallographic preparation techniques were employed to prepare these samples. Coating phase analysis was conducted using an X-ray diffractometer (Smart Lab) under an

Table 1
Chemical composition of QT500-7 (wt.%).

Fe	С	Si	Mn
Bal.	3.5	2.8	0.3

Table 2
Chemical composition of Fe105 powder (wt.%).

I	Fe	Cr	Ni	Nb	Si	С
	Bal.	17.6	2.6	1.2	1.2	0.2

Table 3Chemical composition of Inconel625 powder (wt.%).

Ni	Cr	Fe	Мо	Si	Nb
Bal.	20.4	2.6	8.3	0.2	3.6

accelerating voltage of 40 kV and a current of 40 mA with Cu K α radiation. The scanning parameters included a speed of $2^\circ/\text{min}$, a step size of 0.02° , and a scanning range from 20° to 90° . The microstructure of the coatings was examined using a 3D microscope (LEXT OLS4100, Japan), while detailed microform analysis was performed using a field emission scanning electron microscope (JSM-7800F). Additionally, the elemental distribution within the coatings was characterized by using energy-dispersive spectrometer (EDS) at a working distance of 10 mm and an operating voltage of 15 kV.

2.3. Characterization

The electrochemical behavior of the cladding coatings was evaluated at room temperature using a three-electrode electrochemical workstation (Gamry Reference 600). The experiments were conducted in a 3.5 wt% NaCl aqueous solution to replicate seawater conditions. The three-electrode configuration consisted of the sample as the working electrode, a platinum wire as the counter electrode, and a saturated calomel electrode (SCE) as the reference electrode. Before testing, the sample surfaces were polished with sandpaper (grit 800–2000) and immersed in the solution for 40 min to establish a stable open circuit potential (OCP). Corrosion potentials were measured over a range of potentiondynamic polarization curves recorded at a scan rate of 1 mV/s. To ensure reproducibility, at least three electrochemical measurements were conducted for each sample.

The microhardness of the coatings was measured on polished cross sections using a Vickers microhardness tester (HV-1000, China) equipped with an autofocus system. Measurements were conducted with a load of 3 N and a dwell time of 10 s, with a spacing of 200 100 µm in the central region of the sample. To evaluate the overall wear behavior of the coatings, a multi-functional material surface property tester (MFT-4000, China) was employed. Dry sliding wear tests were conducted at multiple cross-sectional locations, as illustrated in Fig. 3, using ϕ 5 mm counterpart balls with a hardness exceeding 90 HRC were selected for the Al_2O_3 coatings. The tests were performed under a 10 N load, a sliding distance of 5 mm, a rotational speed of 200 rpm, and a duration of 30 min. Wear characterization included analysis of 2D and 3D wear surfaces and volume loss (V-loss) at various points on the coatings, along with calculation of the wear rate (ω), expressed in mm³/N/m, where F represents the loading force and L the total sliding distance. A laser confocal microscope (OLS4000) was employed to examine the wear surfaces with high precision. Due to the relatively small wear loss compared to the sample mass, errors in volume loss measurements were minimized by the advanced data processing capabilities of the confocal microscope. To ensure the reliability of results, all tests were repeated at least twice, and average values were reported.

3. Results and discussion

3.1. Phase analysis

Fig. 4 presents micrographs of the bonding interface in Fe-based coatings with varying Inconel 625 contents (0 wt%, 15 wt%, 30 wt%),



Fig. 1. The SEM morphology of the elemental powders employed in the fabrication of coatings.

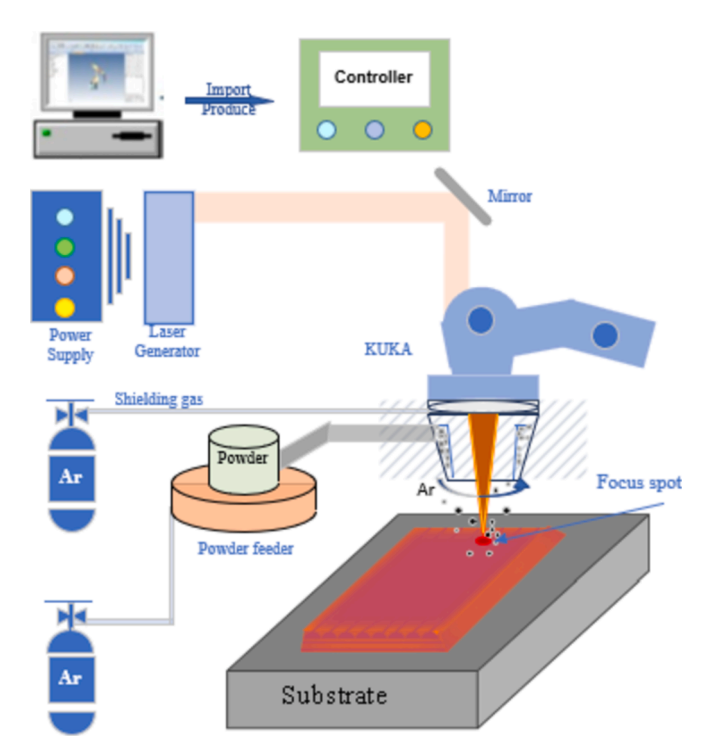


Fig. 2. The fabrication process of coating by powder-fed laser cladding.

 Table 4

 Sample numbers and corresponding material contents.

Sample No.	Material Content
S1	100 wt% Fe105
S2	85 wt% Fe105 and 15 wt% Inconel625
S3	70 wt% Fe105 and 30 wt% Inconel625

shown as S1, S2 and S3 respectively. In the absence of Inconel 625, significant graphite nucleation occurs in the matrix, with graphite diffusing into the melted zone. This behavior is attributed to residual graphite spheres persisting during deposition and migrating into the transition zone. Fig. 5 illustrates that incorporating Inconel625 modifies the structural characteristics of the iron-based coating. As the Inconel 625 content increases, the graphite content in the coating deceases. Fig. 5a illustrates that without Inconel 625 exhibits a prominent distribution of needle-like martensitic structures at the cladding interface, particularly in area Z1. This phenomenon can be attributed to the rapid solidification following surface melting, which shifts the eutectic point toward a higher carbon concentration, leading to the formation of a structure resembling white cast iron, as noted by numerous researchers. Fe-based alloys incorporating Inconel 625 exhibit a strong capacity to

impede carbon diffusion in the transition zone during the cast iron cladding process. In Fig. 5a, a limited number of graphite spheres are observed within the cladding layer. Their formation primarily results from the low solubility of elemental carbon in Ni-based alloys, leading to the precipitation of carbon along grain boundaries during cooling. In Fig. 5b, the white reticulation at the substrate disappear, the needle-like martensitic organization at the coating bond is reduced, as shown in Z2, and the substrate is better bonded to the cladding layer. In Fig. 5c, the coating microstructure is characterized by the presence of fine dendritic, mainly many equiaxial crystals as shown in Z3, the interface is well bonded with no graphite diffusion into the coating, which may be due to the fact that more Ni atoms instead of Fe atoms increase the diffusion activation energy of the carbon atoms and thus inhibit the diffusion of the carbon atoms [20]. As the Inconel 625 content increased, the primary diffraction peaks in the XRD patterns of the cladding layer shifted from Fe carbides to Fe-Ni and Fe-Ni-Cr solid solutions, indicating a uniform distribution of coating elements [21]. Under comparable conditions, incorporating a small amount of Ni-based alloy powder demonstrates a superior capacity to control whitening than Fe-based alloy powder.

Fig. 6 illustrates the XRD patterns of Fe-based layers formed with varying compositions, revealing multiple phases: Austenite Fe (JCPDS index 98-000-0259), martensitic $Cr_{22.3}Fe_{0.77}C_6$ (JCPDS index 01-078-1499), austenitic $Cr_{0.19}Fe_{0.7}Ni_{0.11}$ (JCPDS index 33-0397), and $\textit{Fe}_{0.64}\textit{Ni}_{0.36}$ (JCPDS index 00–047-1405) according to Joint Committee on Powder Diffraction Standards (JCPDS). The S1 sample displayed a pronounced martensitic $Cr_{22.3}Fe_{0.77}C_6$ peak, which can be attributed to elemental diffusion at the interface. With the incorporation of Inconel 625, phases in the S2 coatings shifted the phases towards martensitic $C_{0.08}Fe_{1.92}$ and $Fe_{0.64}Ni_{0.36}$. The S3 coating exhibited strong peaks for martensitic $Fe_{0.64}Ni_{0.36}$, resulting from the infiltration of molten cast iron into the Inconel 625 deposition layer. This behavior is influenced by the comparable atomic radii and electronegativity of Ni and Fe, as well as the higher solubility of Ni in Fe, leading to a solid solution structure (Fe, Ni) [10,22]. Consequently, martensitic structures with Ni-substituted atoms became predominant in the Fe-based laser cladding deposits. Additionally, Cr dissolved within the Fe-Ni solid solution, contributing to improved alloy stability.

3.2. Microstructure characterization

Elemental mapping of the S1 coating, as shown in Fig. 7, highlights the distribution of Fe Ni and Cr across the deposited layers and interfaces. Compositional analysis using EDS map scanning reveals that Cr and Fe are uniformly distributed within the deposited layers, while carbon is concentrated in the interdendritic regions, suggesting that carbides are aligned along the dendritic grain boundaries. The source of carbon is primarily attributed to the dissolution of graphite spheres from the substrate. Additionally, the mapping shows that the Ni concentration at the grain boundaries is significantly lower compared to Cr and Fe, reflecting differences in elemental diffusion and solubility during the

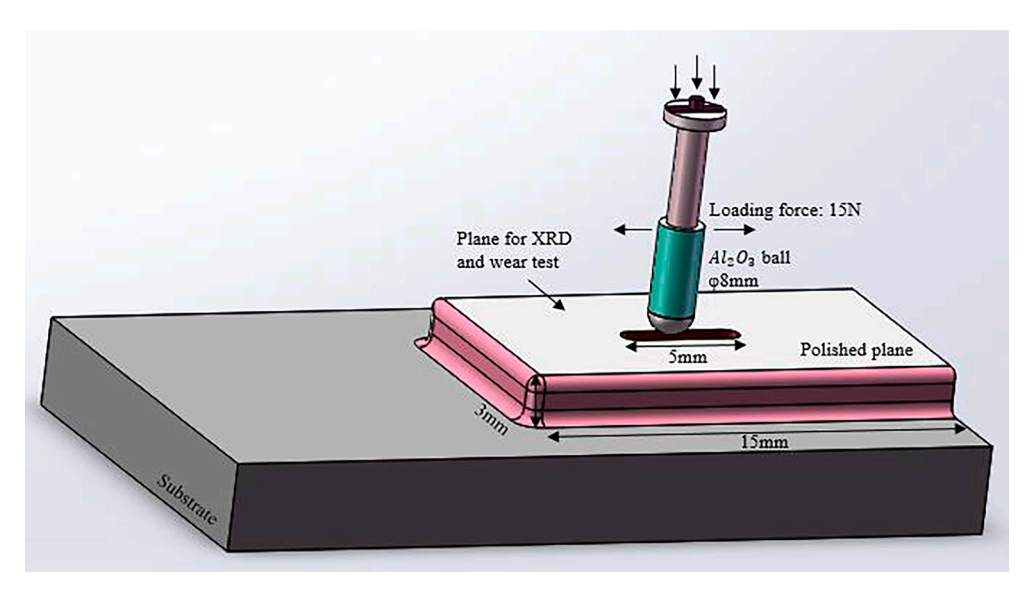


Fig. 3. Schematic diagram of test samples wear resistance process.

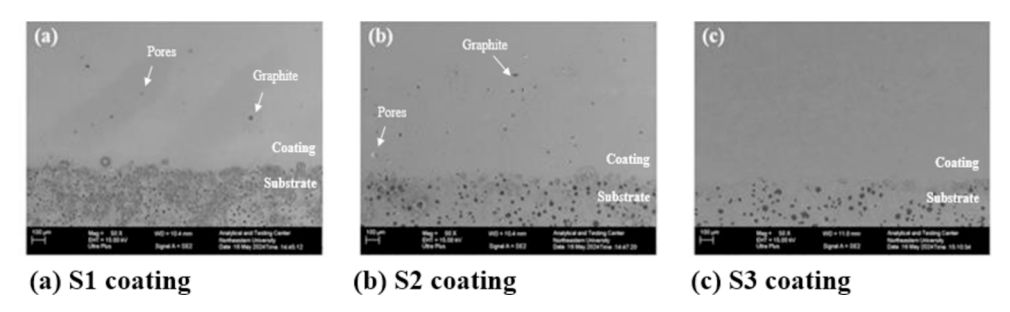


Fig. 4. SEM images of bonding interface (a) S1 coating, (b) S2 coating and (c) S3 coating.

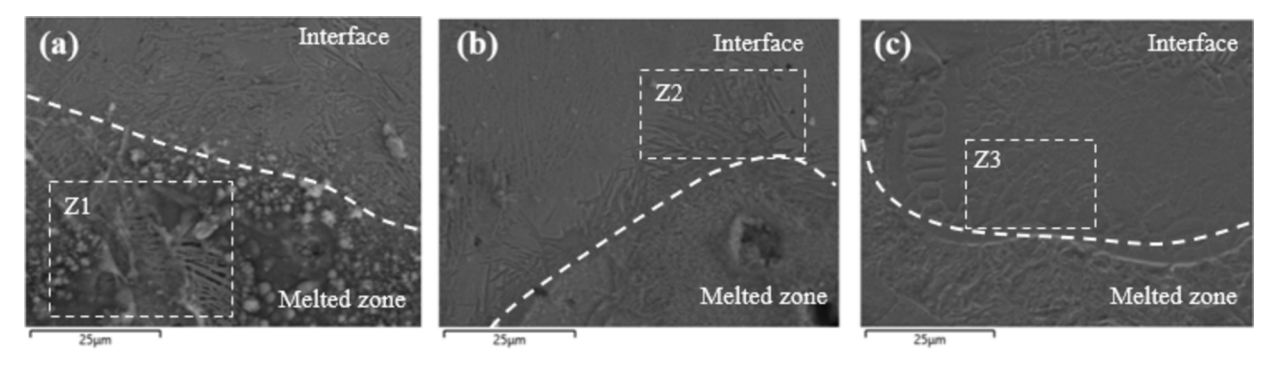


Fig. 5. Laser cladding DI substrate interface (a - c) S1-S3 coatings.

cladding process.

When 15 wt% Inconel 625 particles were added to the raw materials, significant changes in phase morphology and elemental distribution were observed within the S2 coating, as shown in Fig. 8. This coating, prepared using a mixture of 15 wt% Inconel 625 and 85 wt% Fe 105 particles, exhibited a gradual increase in the concentrations of Ni and Cr. Furthermore, Fe, Ni, and Cr were uniformly distributed throughout the coating, consisting with findings from previous studies [23].

Fig. 9 illustrates the significant changes in the phase morphologies and corresponding element distribution within the S3 coating, fabricated with 30 wt% Inconel 625 particles. Compared with Fig. 7 and Fig. 8, a substantial amount of Ni and Cr dissolved into the molten zone. EDS analysis reveals the uniform distribution of Fe, Ni, and Cr throughout the coating. The elevated Ni content enhances solid solution

strengthening and establishes strong metallurgical bonding between the Fe-Ni alloy and the cast iron. Additionally, Cr in solid solution slows the transformation of austenite to ferrite during solidification, thereby increasing the stability of the cladding structure [24]. The reduced carbide content indicates the inhibitory effect of Ni on carbon diffusion.

3.3. Microhardness

Hardness plays a critical role in the remanufacturing of DI, providing insight into certain mechanical properties of the cladding layer. The coating exhibits uniform hardness, attributed to the Ni-based alloy's ability to effectively control carbon diffusion at the forming interface and minimize its impact on the properties of the forming layer. For coating formed with Fe-based alloy powder, interface hardness

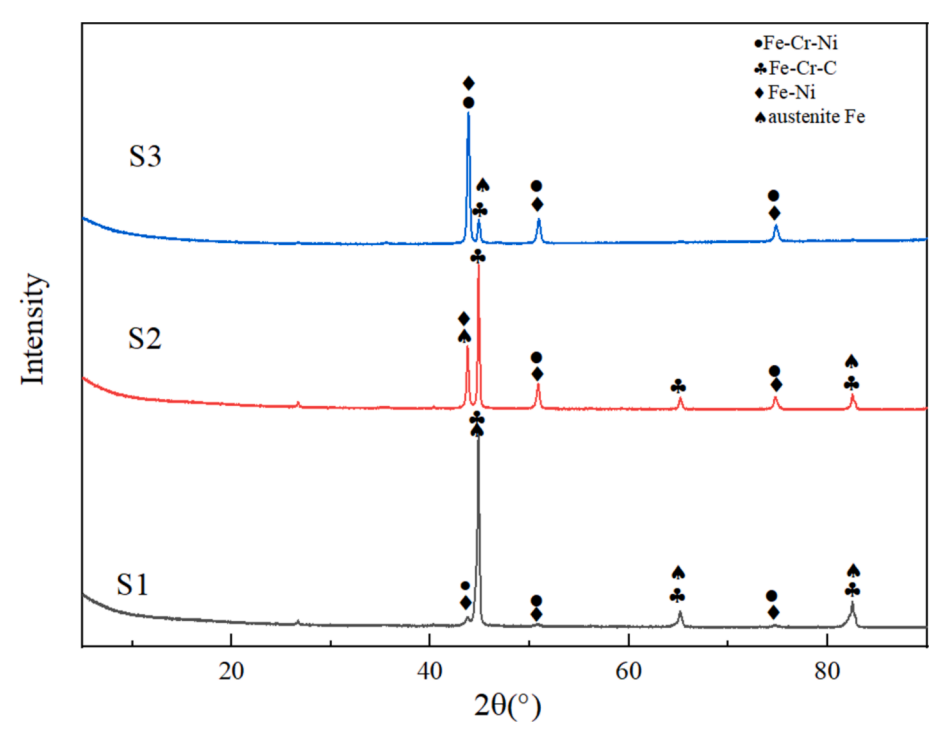


Fig. 6. Comparison among the XRD patterns of Fe 105 coatings fabricated with increasing Inconel 625 wt%.

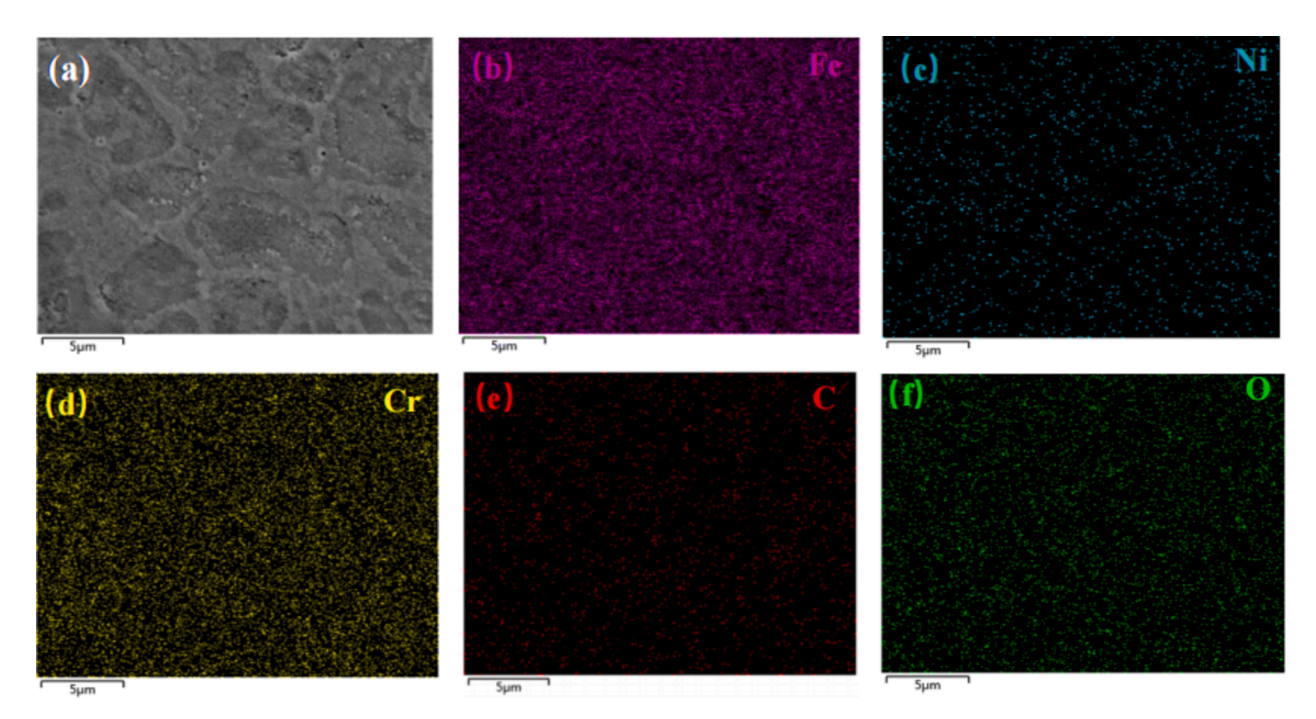


Fig. 7. The distribution of Fe, Ni and Cr elements in S1 coating.

decreases as the number of forming passes and layers increased. Nevertheless, the hardness in the forming layer near the interface remained higher than in regions further away, likely due to the formation of carbide from iron in the forming layer and carbon diffusing from the substrate.

The results indicate that the microhardness of the formed layers exceeds that of the substrate, fulfilling the requirements for remanufacturing. Additionally, the Fe-based alloy coating demonstrates greater hardness than coatings containing Inconel 625. Fig. 10a presents the microhardness distribution of Fe-based and Ni-based alloy surfaces, with

the microhardness values for S1, S2, and S3 being 480, 334, and 304 HV, respectively. The microhardness of the coating with 15 wt% Inconel 625 is 0.7 times that of the Fe-based alloy, while the coating with 30 wt% Inconel 625 is 0.6 times as microhardness. This reduction is primarily due to the substitution of Fe with Ni in the phase, leading to diminished mechanical properties. As illustrated in Fig. 10b, Fe-based alloy powder formation involves Fe and C diffusion from the matrix, resulting in carbide formation within the layer. The hardness of this region is predominantly determined by the molten pool area during the formation process. After the first layer solidifies, the carbon atoms also solidify,

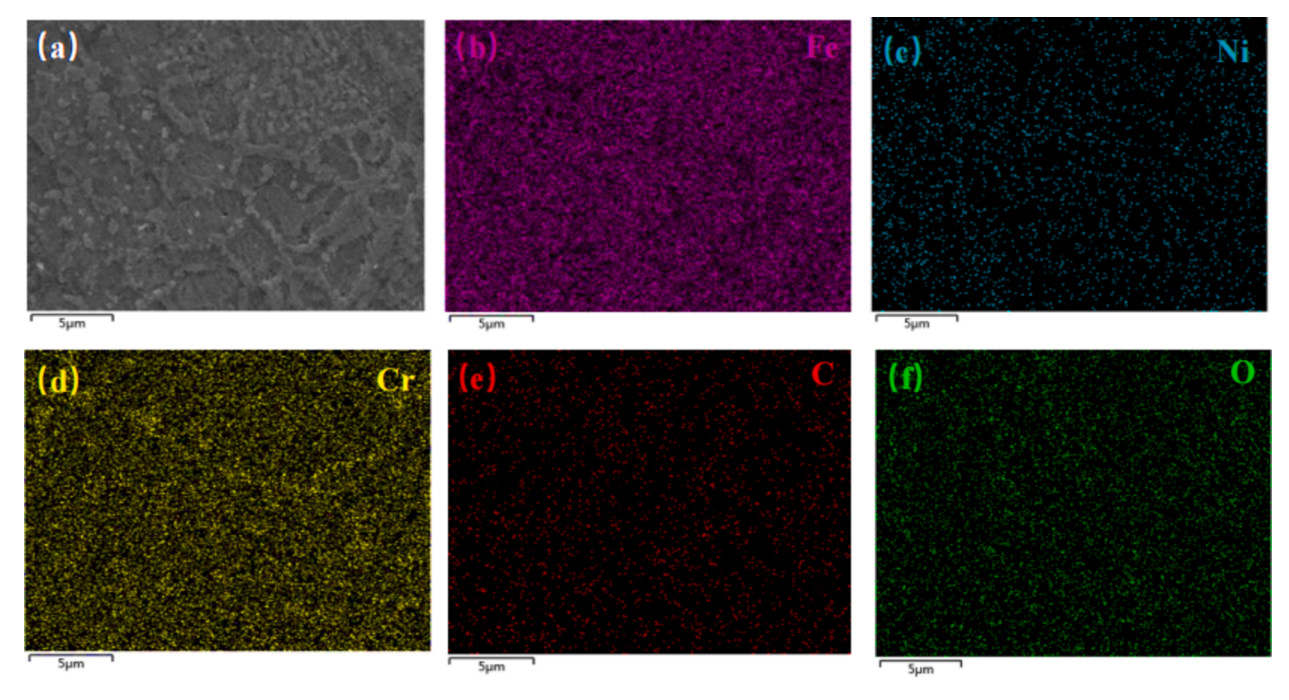


Fig. 8. The distribution of Fe, Ni and Cr elements in S2 coating.

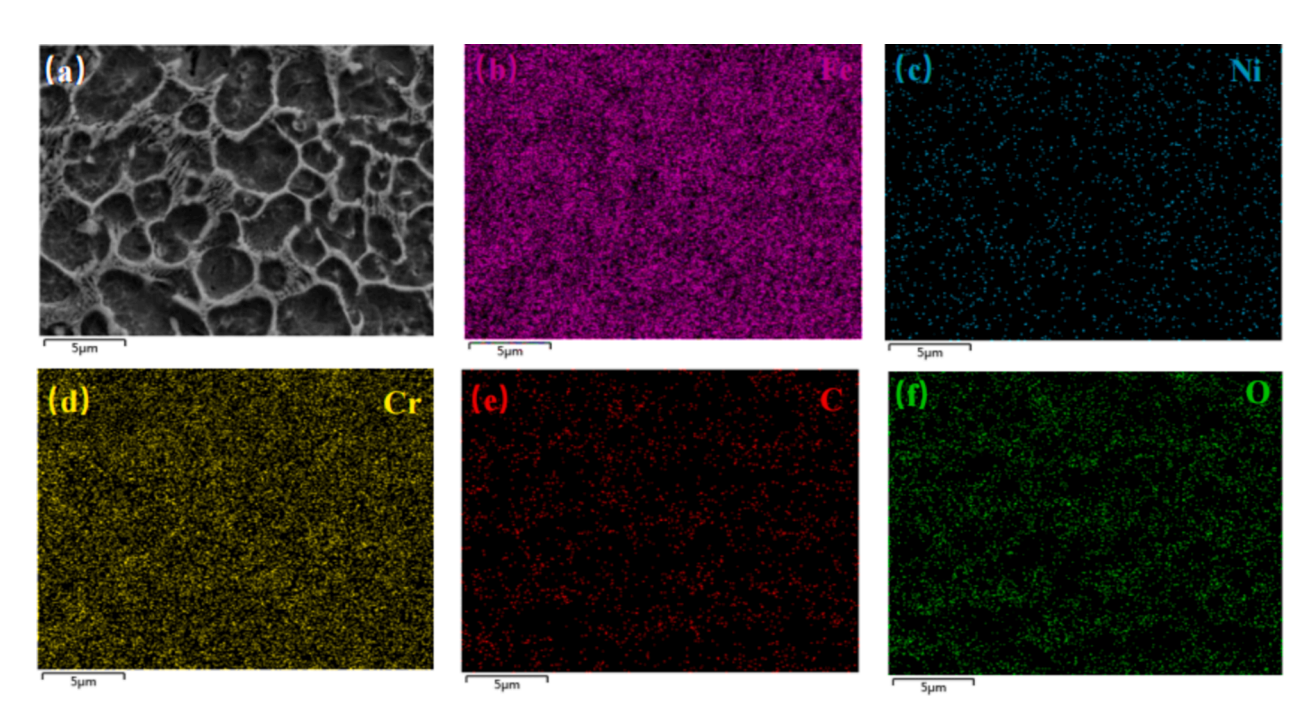


Fig. 9. The distribution of Fe, Ni and Cr elements in S3 coating.

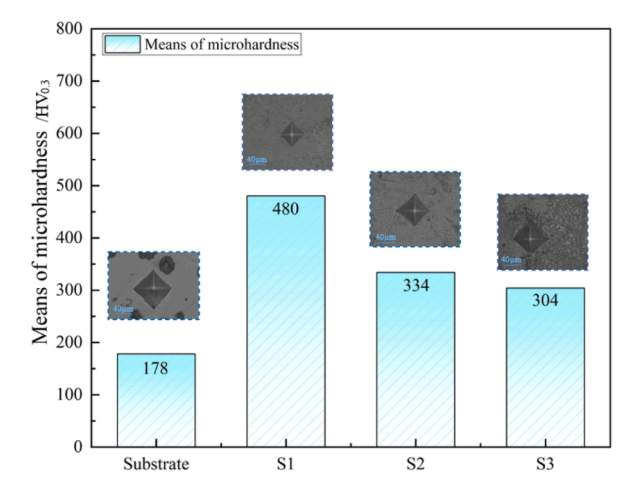
restricting their diffusion in subsequent layers, which decreases the hardness in the subsequent formed layers.

3.4. Corrosion resistance

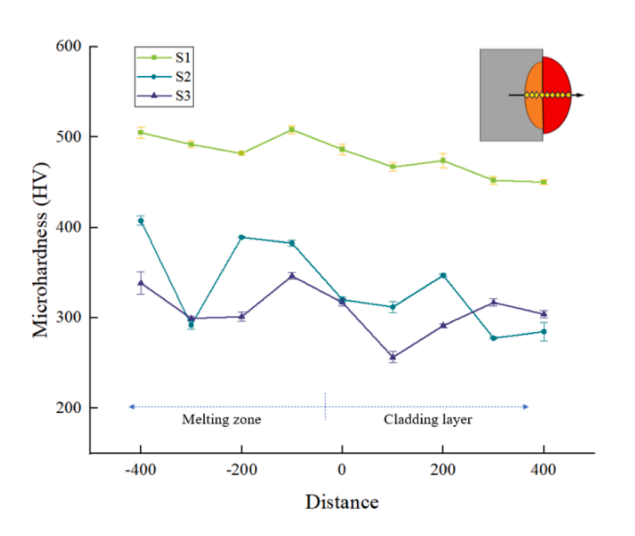
Electrochemical analysis provided substantial evidence of improved corrosion resistance in the coatings. The addition of appropriate amounts of Inconel 625 positively influenced corrosion resistance [25]. Since Fe is more reactive than Ni, the corrosion rate was found to correlate directly with Fe content, while corrosion potential inversely relates to Fe content. Consequently, a reduction in Fe content resulted in increased corrosion resistance [26]. Additionally, the grain size of the

Fe-Ni coatings became more refined, increasing grain boundary density and reducing corrosion susceptibility. Although grain boundaries typically facilitate the diffusion of corrosive elements, the enrichment of Ni and Cr-both highly corrosion-resistant-at the grain boundaries effectively enhanced corrosion resistance in these regions, ultimately boosting the overall corrosion resistance of the coatings.

Fig. 11 shows the results of electrochemical impedance spectroscopy testing. The Nyquist plots display incomplete semicircles, suggesting that the charge transfer mechanism is associated with the electrochemical corrosion process [27]. As shown in Fig. 11(a), a larger impedance arc radius corresponds to higher resistance and enhanced corrosion resistance [28]. The results demonstrate that the impedance



(a) average microhardness of each coating



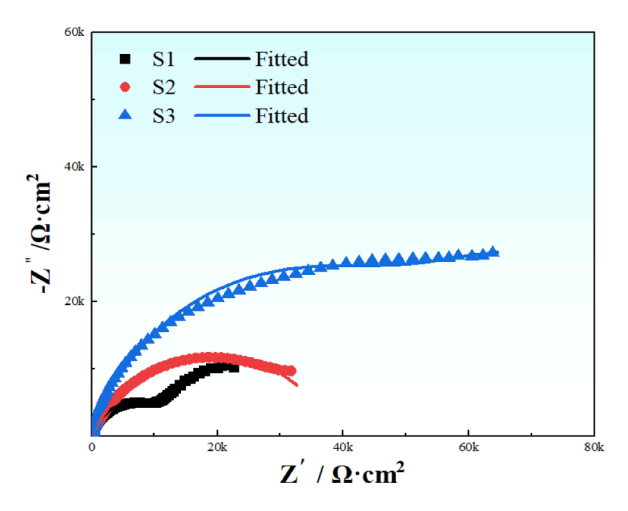
(b) Microhardness distribution along building direction.

Fig. 10. (a) average microhardness of each coating, and (b) Microhardness distribution along building direction.

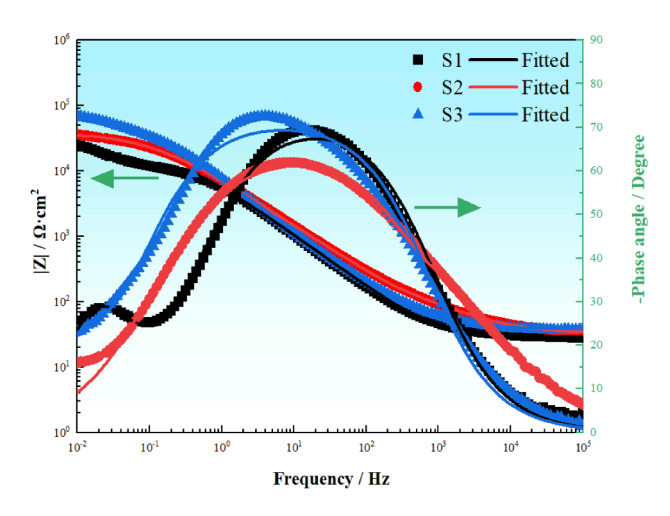
radius increases with the addition of Inconel 625, signifying an improvement in the corrosion resistance of the coating surface as Inconel 625 content rises.

In this equivalent circuit, R_S , R_{film} and R_{ct} represent solution resistance, passivation film resistance and charge transfer resistance, respectively. A constant phase element (CPE) was chosen to fit the impedance profile instead of a simple capacitance, with the aim of better matching the non-flat and rough surfaces of the real electrode and hence a better fit. CPE_{film} and CPE_{dl} represent the passivation film capacitance and the double layer capacitance, respectively. Y_2 is the capacitance parameter. The factor n is frequency independent and is a parameter that characterizes the deviation of the system from the ideal capacitive behavior. The value of n associated with CPE_{film} is in the range $0.5 < n \ll 1$. When n = 0.5, the CPE is expressed as the Warburg impedance associated with the ionic flux through the film. R_f is defined as the total polarization resistance [29].

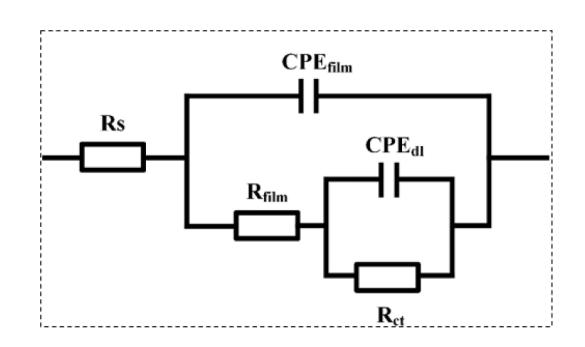
Table 5 illustrates the fitting results of electrochemical impedance spectroscopy. The fitting results also show that the total polarization resistance of S3 is more than three times higher than that of S1, indicating better corrosion resistance of S3 specimens.



(a) Nyquist plots of as-deposited samples.



(b) Bode plots of as-deposited samples.



(c) Equivalent circuit.

Fig. 11. Electrochemical impedance spectroscopy analysis of samples tested in the simulated solution: (a) Nyquist plot, (b) Bode-phase plot, and (c) Equivalent circuit.

3.5. Wear resistance

The wear resistance of Fe- Inconel 625 composites was assessed in this study through evaluations of the friction coefficient, wear volume and worn surface morphology. Fig. 12 presents the friction coefficient (COF) curves for specimens with varying compositions. Fig. 13 shows the wear volume and average friction coefficient of the sampes. Initially, the COF rose rapidly above 0.5, followed by fluctuations as the test

Table 5Fitting results of electrochemical impedance spectroscopy.

Samples		R _{film}	CPE_{film}	CPE_{film}		CPE _{dl}		$R_{ m f}$	χ ²
	(Ω·cm²)	(Ω·cm ²)	$(\Omega^{-1} \cdot \mathbf{s}^{\mathbf{n}} \cdot \mathbf{cm}^{-2})$	n	(Ω·cm²)	Y_2 $(\Omega^{-1} \cdot s^n \cdot cm^{-2})$	n	(kΩ·cm²)	10^{-3}
S1 S2	30.83 32.61	13,002 224.9	$\begin{array}{l} 3.23 \times 10^{-5} \\ 2.94 \times 10^{-5} \end{array}$	0.81 0.68	20,989 38,757	$\begin{array}{c} 5.14 \times 10^{-4} \\ 6.04 \times 10^{-6} \end{array}$	0.92 0.82	33.99 38.98	1.6 1.2
S3	39.77	66,022	3.00×10^{-5}	0.80	36,044	$5.18 imes 10^{-4}$	0.95	102.07	6.5

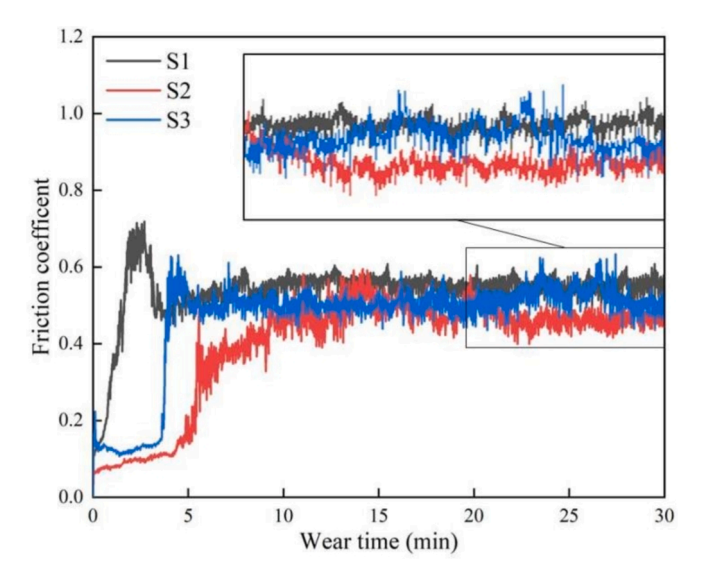


Fig. 12. COF vs. time curves of different coating.

duration increased, eventually stabilizing between 0.50 and 0.70. During the final 10 min, the COF trend became smoother, enabling the calculation of average COF values for the composite coatings over the 20–30-minute wear period. The average COFs for samples S1, S2, and S3 were recorded as 0.5500, 0.4670, and 0.0522, respectively. Notably, despite S1's higher COF, its volumetric removal rate was significantly lower than that of the other coatings, suggesting that Inconel 625 content plays a substantial role in the wear mechanism. Additionally, S2 has

the highest COF, and S3 the lowest hardness, indicating that factors beyond hardness contribute to wear resistance.

Fig. 14(a1-c1) shows an optical image of the wear of the samples (S1-S3) respectively. Large black debris coverings were found on the surfaces of all three samples, and the wear marks were all grooved with large amounts of black abrasive debris. Fig. 14(a2-c2) shows the corresponding 2D color wear pattern corresponding with Fig. 14(a1-c1), and it can be seen that Fig. 14a2 has a large amount of abrasive grains. The wear area expands with the addition of Inconel 625.

To examine the wear mechanisms in specimens of different compositions, SEM observations of the wear scars, as shown in Fig. 15, revealed numerous chips, cracks, delaminations, and grooves on the worn surfaces. Notably, the addition of Inconel 625 improved coating wear resistance, with optimal resistance achieved at 15 wt% Inconel 625. However, when adding 30 wt% Inconel 625, surface damage occurred, increasing the friction coefficient as plastic deformation became the dominant wear mechanism. The wear mechanism models are shown in Fig. 16 and Fig. 17. In sample S1, abrasive wear is the primary wear mechanism, characterized by typical hard-hard contact between friction surfaces, with slight grooves and wear debris forming on the wear track from sliding friction. In sample S2, adhesive wear is evident as wear debris migrates, with some spalling occurring along the wear track edges in the friction direction. The relatively flat overall surface indicates a marked improvement in wear resistance.

For sample S3, fewer surface grooves suggest a decrease in abrasive wear, as plastic deformation prevails over material transfer. The larger and more variable friction coefficient in the Inconel 625 coating is due to Ni's tendency for intermittent adhesive interactions and plastic deformation under grinding ball contact, leading to increased resistance to the grinding balls. In this context, plastic deformation dominates the wear behavior, with large areas of detachment evident on the cladding.

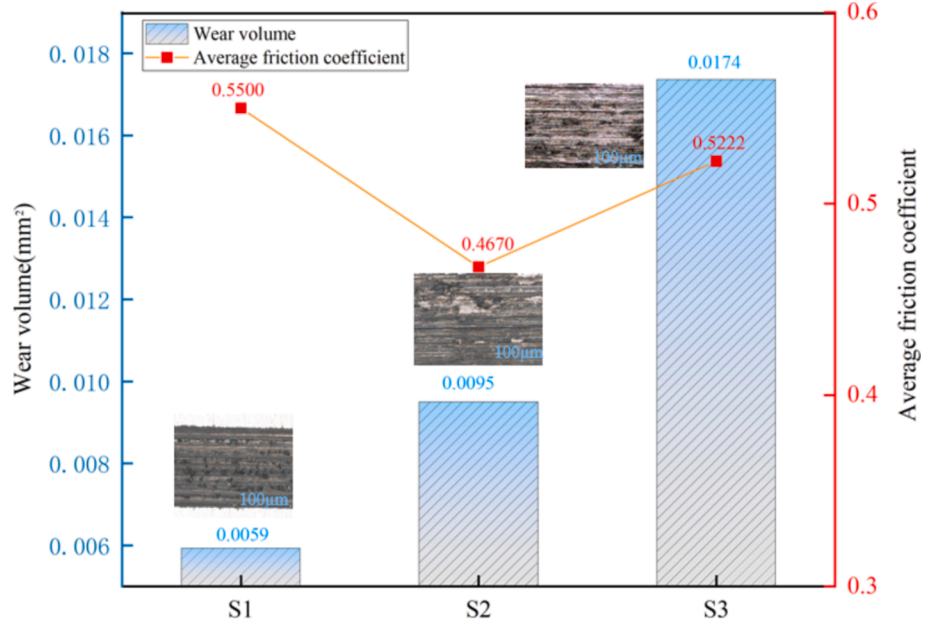


Fig. 13. The COF and volume loss.

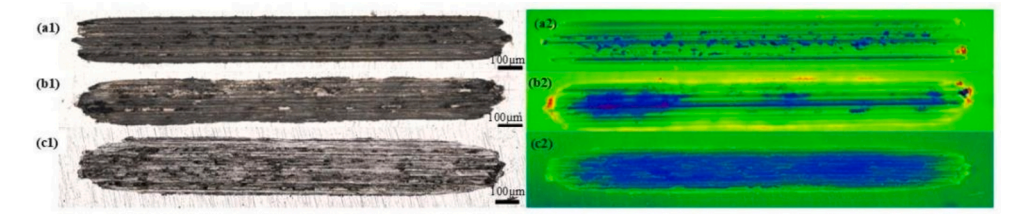
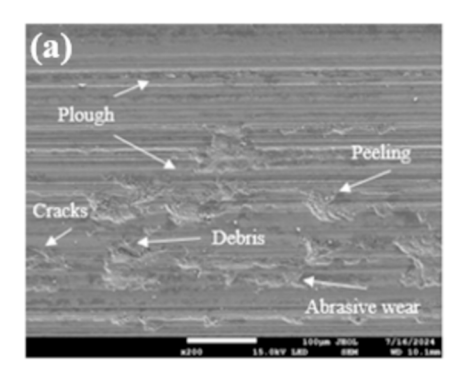
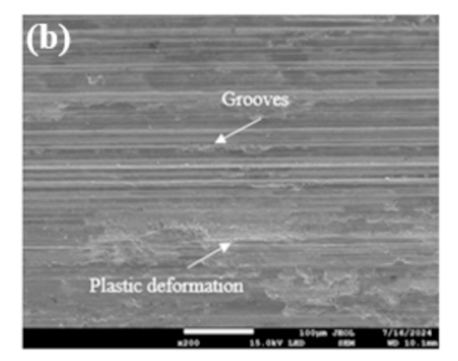


Fig. 14. Optical image of 2D worn surface and 2D color worn surface morphologies.





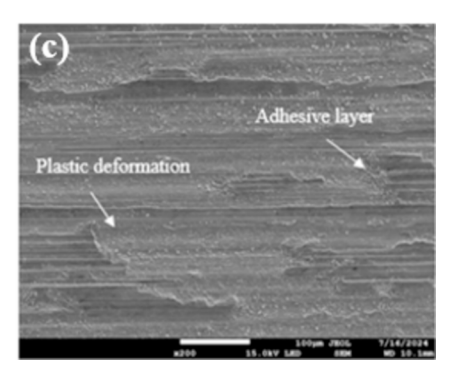


Fig. 15. SEM images of 2D worn surface (a) S1 coating (b) S2 coating and (c) S3 coating.

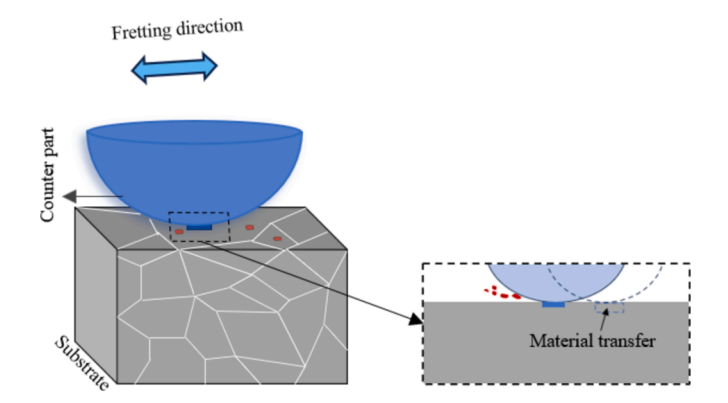


Fig. 16. The schematic diagram of the effect of Fe105 coating on the wear process.

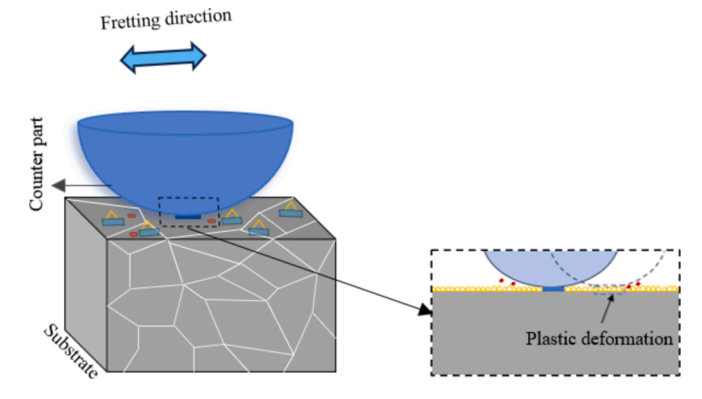


Fig. 17. The schematic diagram of the effect of additional Inconel625 content of Fe105 coating on the wear process.

Key characteristics of this plastic deformation mechanism include extensive surface deformation and localized melting, which cause significant surface damage, though not necessarily producing large amounts of loose debris.

4. Conclusion

In this study, Fe-Inconel 625 composite coatings were fabricated using laser cladding technology, and their corrosion behavior as well as friction and wear characteristics were systematically investigated.

- This study establishes the feasibility of incorporating Inconel 625 into Fe-based alloys to enhance mechanical performance. The appropriate addition of Inconel 625 effectively isolates graphite, preventing the formation of brittle and hard reticulated white-mouth tissue along the edges of the fused cladding, as observed with traditional Fe-based alloy laser cladding.
- Microstructural analysis revealed that defect-free Fe-based coatings can be achieved on the DI substrates with the inclusion of 30 wt% Inconel 625. These coatings exhibit robust metallurgical bonding at the interface, free from macroscope defects such as porosity or cracks.
- 3. The addition of 30 wt% Inconel 625 significantly enhances corrosion resistance to three times that of Fe-based coatings, primarily due to the increased concentration of NiCr elements in the coatings.
- 4. Mechanical property assessments indicated that incorporating 30 wt % Inconel 625 enhanced the hardness of the coatings to 1.7 times that of the substrate. Furthermore, the wear mechanism transitioned from abrasive wear to adhesive wear, highlighting the role of Inconel625 in improving the wear resistance of Fe-based coatings.

$CRediT\ authorship\ contribution\ statement$

Yiqi Wang: Writing – review & editing, Writing – original draft, Methodology, Investigation, Formal analysis, Conceptualization. Tianbiao Yu: Supervision, Project administration, Funding acquisition. Jiayu Sun: Visualization, Data curation. Yingying Zhang: Writing – review & editing, Validation. Zhengyu Sun: Visualization. Chong Yu: . Jiahui Yin: Investigation.

Declaration of competing interest

The authors declare the following financial interests/personal relationships which may be considered as potential competing interests: [Reports a relationship with that includes:. Has patent pending to. If there are other authors, they declare that they have no known competing financial interests or personal relationships that could have appeared to influence the work reported in this paper.].

Acknowledgments

This work was supported by the National Natural Science Foundation of China [Grant number 52075088], Liaoning - Provincial Key Laboratory o-

f Large Equipment Intelligent Design and Manufacturing Technology [Grant number 18006001].

Data availability

The data that has been used is confidential.

References

- C. Liu, et al., Mechanical and tribological behavior of dual-phase ductile iron with different martensite amounts, Journal of Materials Research and Technology-Jmr&t 24 (2023) 2978–2987.
- [2] R. Winiczenko, M. Kaczorowski, Friction welding of ductile iron with stainless steel, J. Mater. Process. Technol. 213 (3) (2013) 453–462.
- [3] Y. Yürektürk, M. Baydogan, Characterization of ferritic ductile iron subjected to successive aluminizing and austempering, Surf. Coat. Technol. 347 (2018) 142, 140.
- [4] S.J. Deng, et al., Study on the mechanism and correlation of double-pit pitting in ductile iron IN625 laser cladding layer, Journal of Adhesion Science and Technology 38 (14) (2024) 2584–2620.
- [5] N. Ochoa, et al., Pseudo-passive films on cast irons: a strategy to mitigate corrosion by acting directly on microstructure. Corros. Sci. 206 (2022).
- [6] K.Y. Benyounis, et al., Surface melting of nodular cast iron by Nd-YAG laser and TIG, J. Mater. Process. Technol. 170 (1–2) (2005) 127–132.
- [7] X. Yang, et al., Investigation of nanomechanical properties and thermal fatigue resistance of gray cast iron processed by laser alloying, J. Alloy. Compd. 626 (2015) 260–263.
- [8] Sun, G.F., et al. Laser surface alloying of NiCr-Cr₃C₂ and C-B-W-Cr powders on nodular cast iron rolls. in 2nd International Conference on Multi-Functional Materials and Structures. 2009. Qingdao, PEOPLES R CHINA.

- [9] X.X. Luo, et al., Enhanced corrosion resistance properties of Fe-Al-Cr laser cladding coatings on 1045 carbon steel substrates, Heliyon 9 (3) (2023).
- [10] G. Jie, et al., Effect of Fe content on microstructure and corrosion resistance of Nibased alloy formed by laser cladding, Surf. Coat. Technol. 446 (2022).
- [11] N. Catalán, et al., Surface Laser Treatment of Cast Irons, A Review. Metals 12 (4) (2022).
- [12] Y.J. Li, et al., Surface remanufacturing of ductile cast iron by laser cladding Ni-Cu alloy coatings, Surf. Coat. Technol. 347 (2018) 20–28.
- [13] T.Q. Chen, et al., In-situ observation and kinetics study on shrinkage defect corrosion of ductile iron in NaCl solution, Corros. Sci. 232 (2024).
- [14] Z.K. Weng, et al., Diode laser cladding of Fe-based alloy on ductile cast iron and related interfacial behavior, Surf. Coat. Technol. 286 (2016) 64–71.
- [15] T. Poloczek, A. Lont, J. Górka, The structure and properties of laser-cladded inconel 625/TiC composite coatings, Materials 16 (3) (2023).
- [16] T. Poloczek, A. Lont, J. Gorka, Structure and properties of laser-cladded Inconel 625-based in situ composite coatings on S355JR substrate modified with Ti and C powders, Mater. Sci.-Pol. 40 (4) (2022) 14–27.
- [17] H. Yan, et al., Microstructure and wear resistance of composite layers on a ductile iron with multicarbide by laser surface alloying, Appl. Surf. Sci. 256 (23) (2010) 7001–7009.
- [18] D.W. Zeng, et al., Corrosion resistance enhancement of Ni-resist ductile iron by laser surface alloying, Scr. Mater. 44 (4) (2001) 651–657.
- [19] L.Y. Chen, et al., Effects of CeO2 addition on microstructure and properties of ceramics reinforced Fe-based coatings by laser cladding, Int. J. Adv. Manuf. Technol. 115 (7–8) (2021) 2581–2593.
- [20] X. Wang, et al., Effects of Nickel contents on phase constituent and mechanical properties of ductile iron, Int. J. Met. 18 (3) (2024) 2721–2731.
- [21] M.H. Sohi, et al., Microstructural study of surface melted and chromium surface alloyed ductile iron, Appl. Surf. Sci. 258 (19) (2012) 7348–7353.
- [22] L. Zhou, et al., Microstructure and properties of Fe-Cr-Ni alloy coatings on T10 steel by laser cladding, Mater. Res. Express 7 (1) (2020).
- [23] Y.L. Lei, et al., Surface Alloying characteristics of inconel 625 Coatings deposited on ductile cast iron by plasma wire-arc welding, J. Mater. Eng. Perform. (2023).
- [24] B. Ren, et al., Effect of elemental interaction on microstructure of CuCrFeNiMn high-entropy alloy system (vol 493, pg 148, 2010), J. Alloy. Compd. 503 (2) (2010) 538
- [25] L.Y. Bai, et al., High temperature chloride corrosion behavior of 904L:AlFeNiMoNb High-Entropy Alloy, Front. Mater. 8 (2021).
- [26] W.R. Shen, et al., Effect of Laser on Abnormal Reduction Process and properties evaluation of electrodeposited soft magnetic Fe-Ni Coating, J. Electrochemical Society 169 (8) (2022).
- [27] J.B. Zhang, et al., Picosecond laser remelting of electrodeposited Ni-P coating: parameters optimization and electrochemical corrosion behavior, Surf. Coat. Technol. 471 (2023).
- [28] L.D. Yu, et al., Influence of laser parameters on corrosion resistance of laser melting layer on C45E4 steel surface, J. Manuf. Process. 91 (2023) 1–9.
- [29] L. Swain, et al., Electrochemical behaviour of LiCl-KCl eutectic melts containing moisture as impurity. part II: Uranium electrode, J. Electroanal. Chem. 907 (2022).